Supporting Information

Rational Design of $RuCu(P_xO_y)$ Nanosheets for Synergistically Enhanced Hydrogen Evolution Reaction in Alkaline Medium

Haiyan Pang,[a] Zheng Tang,[a] Ruohan Huang,[a] Panpan Wang,[a] Xiao Liu,*[ab] and Hongling Liu,*[a] and Yuechang Wei*[c]

[a] *Henan Key Laboratory of Polyoxometalate Chemistry, College of Chemistry and Molecular Science, Henan University, Kaifeng 475001, PR China*

[b] *Henan Province Engineering Technology Research Center of Water Environment and Health, College of Pharmacy and Chemical Engineering, Zhengzhou University of Industrial Technology, Zhengzhou 451150, China*

[c] *State Key Laboratory of Heavy Oil Processing, China University of Petroleum, Chang Ping, Beijing 102249, China*

Experimental Section

Materials. Ruthenium acetylacetonate ($Ru(acac)_3$, 99.9%) and Copper acetate monohydrate ($Cu(ac)_2$, 99%) were purchased from Macklin (Shanghai, China). Red phosphorus, tin (Sn), and tin iodide (SnI_4) were purchased from Aladdin Reagents. Tetrabutylammonium hexafluorophosphate (TBAP, 98%) was purchased from Macklin. N, N-dimethylformamide (DMF, HPLC grade) was purchased from Aldrich (Beijing, China). Ethanol was purchased from Tianjin Fuyu fine CHEMICAL Co., Ltd. (Tianjin, China), respectively. All chemicals were purchased commercially without further refinement.

Synthesis of bulk BP. Bulk BP was prepared according to the literature. Typically, red

phosphorus (500 mg), Sn (20 mg), and SnI_4 (10 mg) were sealed in a quartz tube. The tube was heated to 923 K with a heating ramp rate of about 1.35 K per min and kept on for five hours. Then, the tube was ramped down to 773 K with rate of 0.33 K per min, followed by a natural cooling process. The large BP crystals were collected and washed with hot toluene and acetone for several times to remove the residual mineralizer. After being dried under vacuum, the product was kept in a glovebox for further analysis.

Synthesis of BP nanosheets: The BP nanosheets were prepared by an electrochemical exfoliation method. 2 g tetrabutylammonium hexafluorophosphate was dissolved in 40 mL DMF as electrolyte solution. The block BP crystal is connected to the negative electrode by a fixture, and the Pt sheet is connected to the positive electrode. After the electrodes were immersed in the electrolyte, a potential of -12 V was applied to them. Due to the insertion of TBA^+ ions, the bulk BP rapidly swelled. When the current on the BP electrode stops decreasing, the stripping ends. Then, the material was gently removed from the clamp and washed by DMF 5 times. Subsequently, the washed BP was dispersed in DMF and sonicated for 4 h. To obtain ultra-thin BP nanosheets, the dispersion was centrifuged for 20 min at 1000 rpm and the precipitate was removed. Afterward, the few-laver BP nanosheets were collected by centrifugation at 11000 rpm for 20 minutes.

Synthesis of RuCu(P_xO_y) nanosheets. RuCu(P_xO_y) nanosheets were prepared by a simple hydrothermal synthesis method. Firstly, BP nanosheets (0.0050 g), $Ru(acac)_3$ (0.0100 g), $Cu(ac)_2$ (0.0200 g), and 2.5 mL DMF solution were added to the Teflon-lined stainless-steel autoclave. Subsequently, the reactor was positioned within a blast

drying oven and subjected to heating up to 180℃ for 3 h. After cooling down to room temperature, the black products were washed with ethanol many times. Finally, the centrifuged material was placed in a vacuum-drying oven for subsequent use. For comparison, Ru(P_xO_y) was prepared similarly using only $Ru(acac)_3$ as the precursor and BP. Cu(P_xO_y) was prepared similarly using only $Cu(ac)_2$ as the precursor and BP. RuCu was prepared similarly using only $Ru(acac)_3$ and $Cu(ac)_2$ as the precursor.

Electrochemical measurement of RuCu(P_xO_y) nanosheet: The electrochemical measurements were tested at room temperature by a Donghua DH 7000C electrochemical workstation with a typical three-electrode setup, using the glassy carbon electrode modified with RuCu(P_xO_y) nanosheets as the working electrode, a graphite rod as the counter electrode. In an acidic electrolyte, the Hg/Hg_2Cl_2 electrode was applied to the reference electrode. In alkaline electrolyte, Hg/HgO was served as the reference electrode. 2 mg of RuCu(P_xO_y) nanosheets were dissolved in a mixed solution of 380 μl isopropanol and 20 μL Nafion, and ultrasounded for 1 h to form a uniform ink. A 20 μL catalyst ink droplet was dried on a glassy carbon electrode with a diameter of 3 mm, and its geometric area was 0.07065 mg cm^{-2}. HER measurements were conducted in 0.5 mol L^{-1} H_2SO_4 and 1.0 mol L^{-1} KOH aqueous solution. All of the overpotentials were calibrated with respect to the reversible hydrogen electrode: in acidic electrolyte, E (vs. RHE)=E (vs. Hg/Hg_2Cl_2) + 0.242 + 0.0591 V × pH, while in alkaline electrolyte, E (vs. RHE)=E (vs. Hg/HgO) + 0.098 + 0.0591 V × pH. The HER performance of the catalyst was tested by electrochemical experiments such as cyclic voltammetry (CV), linear sweep voltammetry (LSV), chronopotentiometry (CP) and

electrochemical impedance spectroscopy (EIS). The scan rate of linear sweep voltammetry is 2 $mV \cdot s^{-1}$. Tafel slopes were calculated based on the corresponding LSV curves. EIS was carried out at a rated voltage in the frequency range of 0.01 Hz-1000000 Hz. CV tests were carried out at different scan rates of 20, 40, 60, 80, 100 $mV \cdot s^{-1}$ in the non-faradaic range to obtain the double-layer capacity (C_{dl}). The stability of the catalyst was tested by CV technique for 1000 cycles and chronoamperometry method at the current density of 10 $mA \cdot cm^{-2}$. The turnover frequency (TOF) value was obtained by the formula: TOF = jA/nFN, where j is the current density, n is 2, F is the Faraday constant 96485 $C \cdot mol^{-1}$, and N is the number of catalytic active sites on the electrode (mol). All current density values are normalized according to the geometric area of the working electrode.

Characterization. The structure of RuCu(P_xO_y) nanosheets was investigated using X-ray diffractometry (XRD, X' Pert Pro, Bruker with Cu *Ka* radiation, Karlsruhe, Germany, 2θ = 5°~90°). The morphologies of RuCu(P_xO_y) nanosheets were obtained via transmission electron microscopy (TEM, JEOL JSM-7610F PLUS, JEOL Ltd., Tokyo, Japan). The contents of Ru and Cu in the samples were received by inductively coupled plasma mass spectrometry (ICP-MS) with a PerkinElmer NexION 300X. X-ray photoelectron spectroscopy (XPS, Thermo Fisher Scientific, Waltham, Escalab 250 MA, USA) was used to study the surface compositions. Raman spectra (XploRA, Jobin-Yvon) were recorded with a solid-state laser at the excitation wavelength of 532 nm. The Fourier transform infrared spectroscopy (FTIR, Nicolet Company, USA) studied RuCu(P_xO_y) nanosheets in the wavelength range of 500 ~ 4000 cm^{-1}.

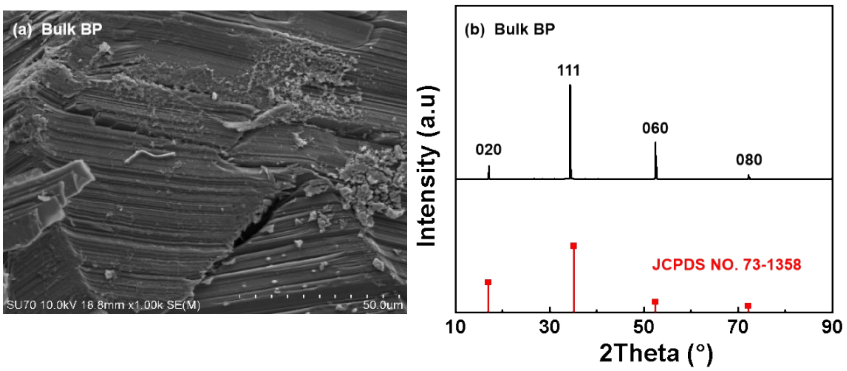

Fig. S1. (a) SEM image of the as-prepared bulk BP showing the layered structure of BP. (b) XRD patterns of the as-prepared bulk BP. Bar diagram for the JCPDS of BP.

The SEM image of the synthesized bulk BP reveals its layered morphology. XRD analysis demonstrates diffraction peaks matching the orthorhombic crystal structure of BP. The diffractions peaking at 16.9°, 35°, and 52.3° are accurately assigned to (020), (111), and (060) planes of the bulk BP. These findings confirm the effective synthesis of well-crystalline bulk BP.

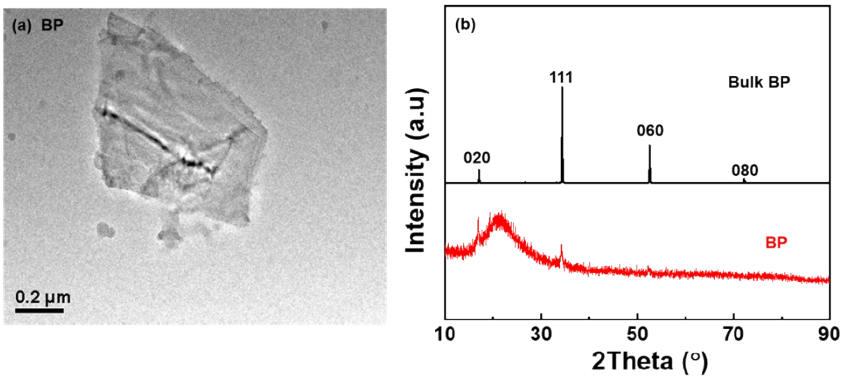

Fig. S2. (a) TEM and (b) HRTEM images of BP. (c) XRD patterns of bulk BP and BP nanosheets.

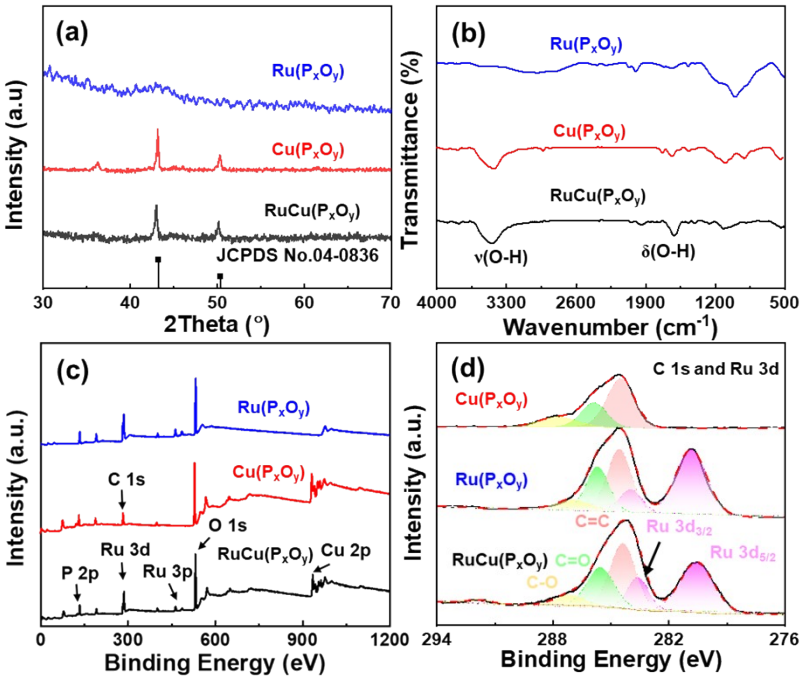

Fig. S3. Structure characterization analyses of the RuCu(P_xO_y) nanosheets. (a) XRD patterns, (b) FTIR spectra, (c) full XPS spectra, and (d) C 1s and Ru 3d HR-XPS spectra.

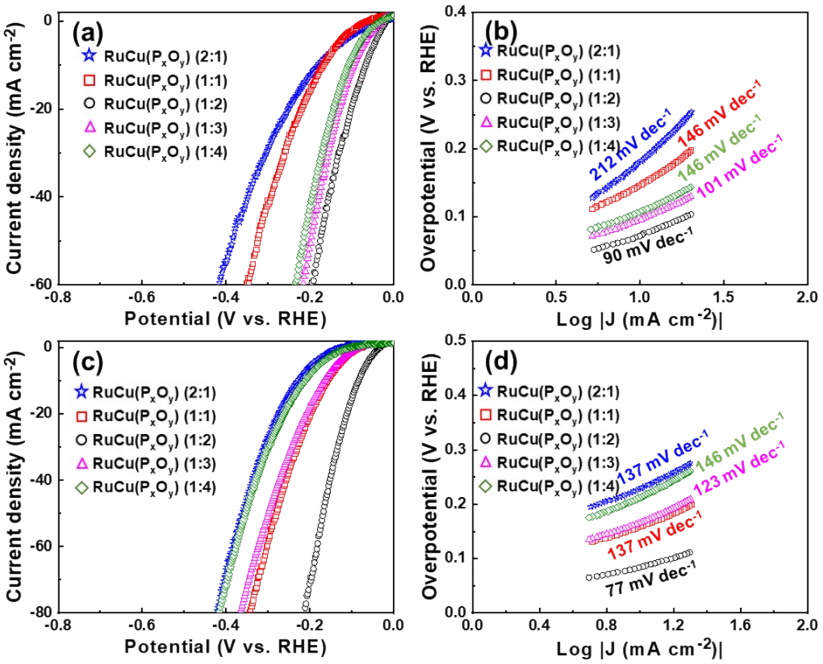

Fig. S4. HER performances of different ratios between metals catalysts in alkaline and acidic mediums. (a) LSV curves in alkaline medium, (b) Tafel plots in alkaline medium, (c) LSV curves in acidic medium, (d) Tafel plots in acidic medium

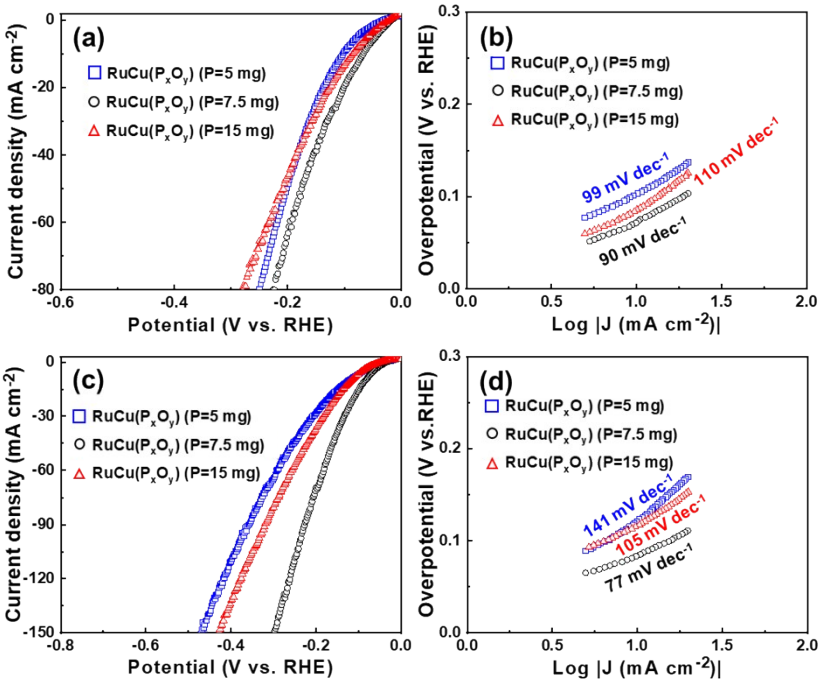

Fig. S5. HER performances of different content of BP nanosheet catalysts in alkaline and acidic medium. (a) LSV curves in alkaline medium, (b) Tafel plots in alkaline medium, (c) LSV curves in acidic medium, (d) Tafel plots in acidic medium.

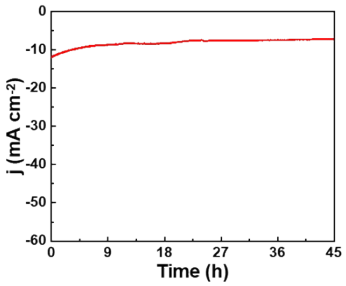

Fig. S6. There were stability tests of RuCu(P_xO_y) nanosheets in an alkaline medium.

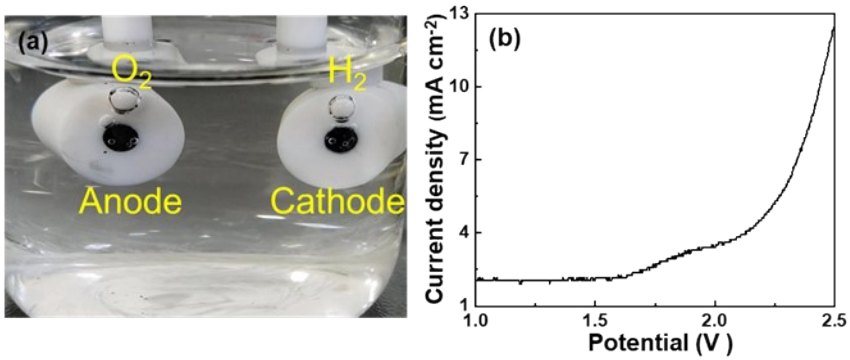

Fig. S7. There was a total water splitting test of RuCu(P_xO_y) nanosheets in alkaline solution. (a) electrolyzed water diagram, (b) LSV.

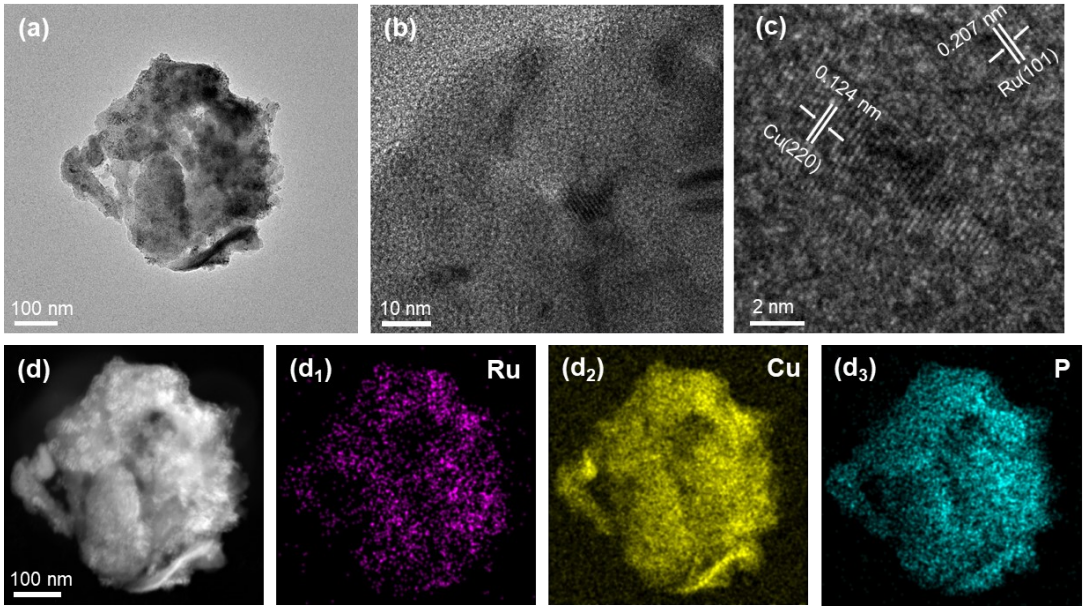

Fig. S8. TEM analyses of the RuCu(P_xO_y) nanosheet after catalytic reaction. (a) TEM image, (b) magnified TEM image, (c) HR-TEM image, and (d) HAADF-STEM and elemental mapping.

It is noted that the catalysts on the electrode surface would undergo irreversible surface reconstruction during the HER process in the alkaline medium[1]. To comprehend this unique feature and obtain a better understanding of the reasons for such electrochemical trends, the RuCu(P_xO_y) catalysts were examined with morphology and structure characterization before and after electrochemical testing. As shown in Fig. S8a, the RuCu(P_xO_y) nanosheet after the catalytic reaction still was a 2D plane structure. However, the enlarged TEM image shows the original tiny particles are gone (Fig. S8b), implying the existence of surface reconstruction, whereas the lattice fringes of RuCu(P_xO_y) nanosheet can be observed (Fig. S8c). The Ru, Cu, and P elements are still evenly distributed on the surface of RuCu(P_xO_y) nanosheets, indicating the integrity of RuCu(P_xO_y) nanosheet elements after electrochemical testing.

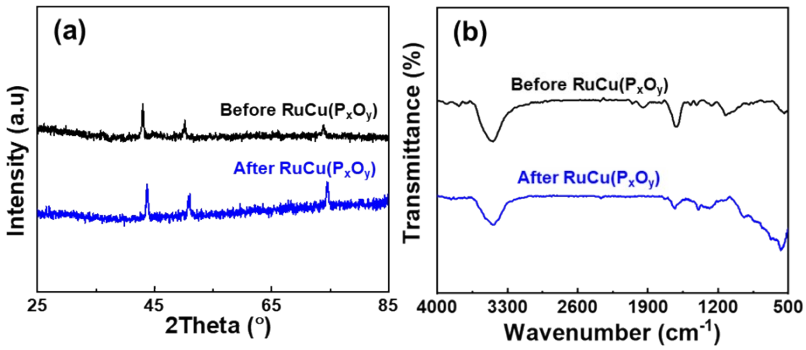

Fig. S9. Structure characterization analyses of the RuCu(P_xO_y) nanosheets after catalytic reaction. (a) XRD patterns, (b) FTIR spectra.

Whereafter, the RuCu(P_xO_y) nanosheets were characterized by XRD and FTIR analysis before and after the HER test. The diffraction peaks of RuCu(P_xO_y) nanosheets located at 43.2°, 50.4°and 73.78° shift to higher diffraction angles (43.72°, 50.99°, and 74.53°), suggesting that dissolution of P element gives rise to d-spacing decreases[2]. In the FTIR spectra, the peak 943.2 cm^{-1} is the stretching vibration of P-O bond. However, these vibrations of the P-O bond disappear, which is most likely due to the dissolution of P element during the HER process[3].

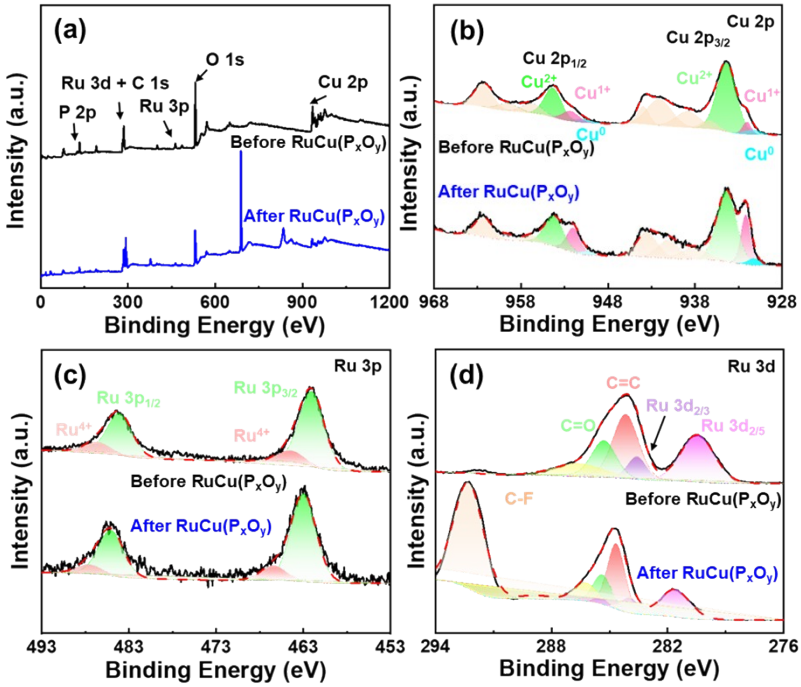

Fig. S10. XPS spectra of analyses of the RuCu(P_xO_y) nanosheets after catalytic reaction. (a) full XPS spectra, (b) Cu 2p HR-XPS spectra, (c) Ru 3p HR-XPS spectra, (d) Ru 3d HR-XPS spectra.

To dig out the variations of the composition and valence state on the surface of the RuCu(P_xO_y) nanosheets during the electrolysis test, XPS measurements before and after the electrolysis test were carried out. The presence of F element arises largely from the electrolyte on the surface of the RuCu(P_xO_y) nanosheets after catalytic reaction, as represented in Fig. S10a. The spectra of Ru 3p (located at 461.7 eV and 483.7 eV ascribed to Ru $3p_{3/2}$ and Ru $3p_{1/2}$) indicates that metallic Ru dominates in the fresh sample, which has a positive shift (462.9 eV and 485.1 eV) after HER tests (Fig. S10b). The reason for such a shift of Ru 3p is probably due to the dissolution of P during the HER process, resulting in the decrease of P electron donors. Based on XPS data, the content of P from 11.7 at% in fresh RuCu(P_xO_y) nanosheets drops down to 6.3 at% in the same sample after the HER test. In addition, the Cu 2p spectra show three valence states Cu^0, Cu^{1+}, and Cu^{2+} on the surface of the sample. More amazingly, the content

of oxidized states (Cu^{2+}) decreased (87.1%→69.8%) greatly. Conversely, the content of metallic (Cu^{1+}) increased (7.5%→25.6%) greatly (Fig. S10c). The increase of (Cu^{1+}) content facilitates the desorption process of H* due to Cu^{+} sites generally exhibiting weaker H* adsorption than Ru sites.

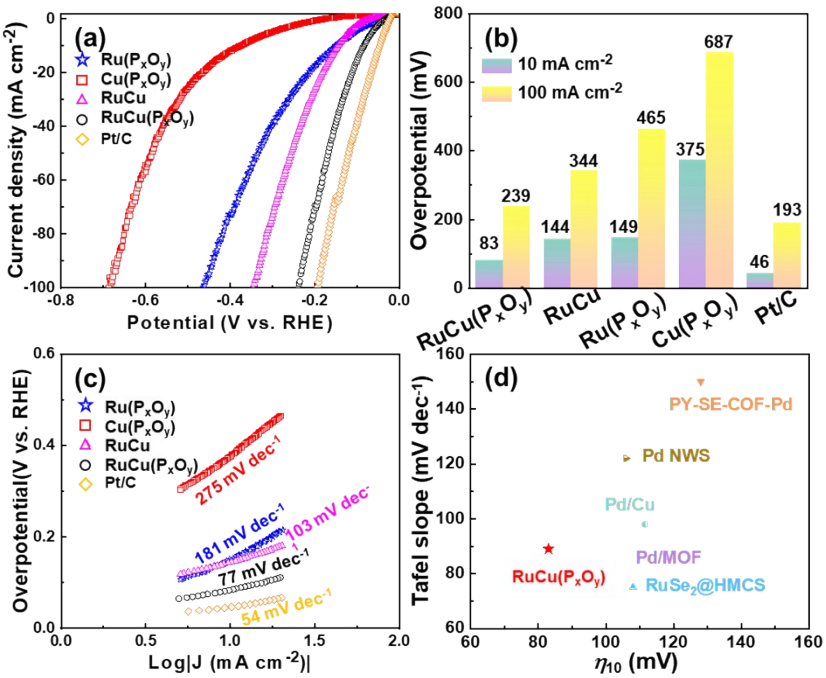

Fig. S11. HER performances of different catalysts ($Ru(P_xO_y)$, $Cu(P_xO_y)$, RuCu, $RuCu(P_xO_y)$ and Pt/C) in an acidic medium. (a) LSV curves, (b) Overpotential at 10 and 100 mA cm^{-2} for HER (c) Tafel plots, (d) Comparison of the overpotentials for HER (at 10 mA cm^{-2}) and Tafel plots of the prepared $RuCu(P_xO_y)$ nanosheets and other reported electrocatalysts.

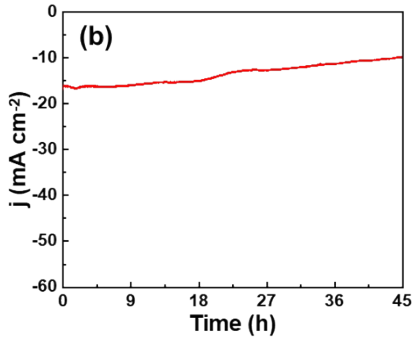

Fig. S12. There were stability tests of RuCu(P_xO_y) nanosheets in an acidic medium.

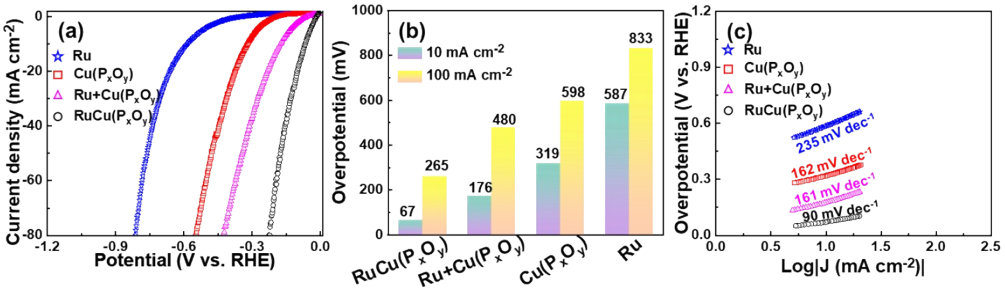

Fig. S13 HER performances of different catalysts (Ru, $Cu(P_xO_y)$, $Ru+Ru(P_xO_y)$, $RuCu(P_xO_y)$) in an alkaline medium. (a) LSV curves, (b) Overpotential at 10 and 100 mA cm^{-2} for HER, (c) Tafel plots.

Obviously, the $RuCu(P_xO_y)$ catalyst exhibits the most superior HER activity with ultralow overpotentials at 10 mA cm^{-2} of 67 mV, which is lower than that of $Ru+Cu(P_xO_y)$ (176 mV), $Cu(P_xO_y)$ (319 mV), and Ru (587 mV). Afterward, the corresponding Tafel slope was obtained. The Tafel slope of $RuCu(P_xO_y)$ (90 mV dec^{-1}) is lower than $Ru+Cu(P_xO_y)$ (161 mV dec^{-1}), $Cu(P_xO_y)$ (162 mV dec^{-1}), and Ru (235 mV dec^{-1}). Although the catalytic performance of $Ru+Cu(P_xO_y)$ (physical mixture) was inferior to that of $RuCu(P_xO_y)$ (chemically bonded), it still outperformed both individual Ru and $Cu(P_xO_y)$ components, suggesting the existence of synergistic effects between the two phases.

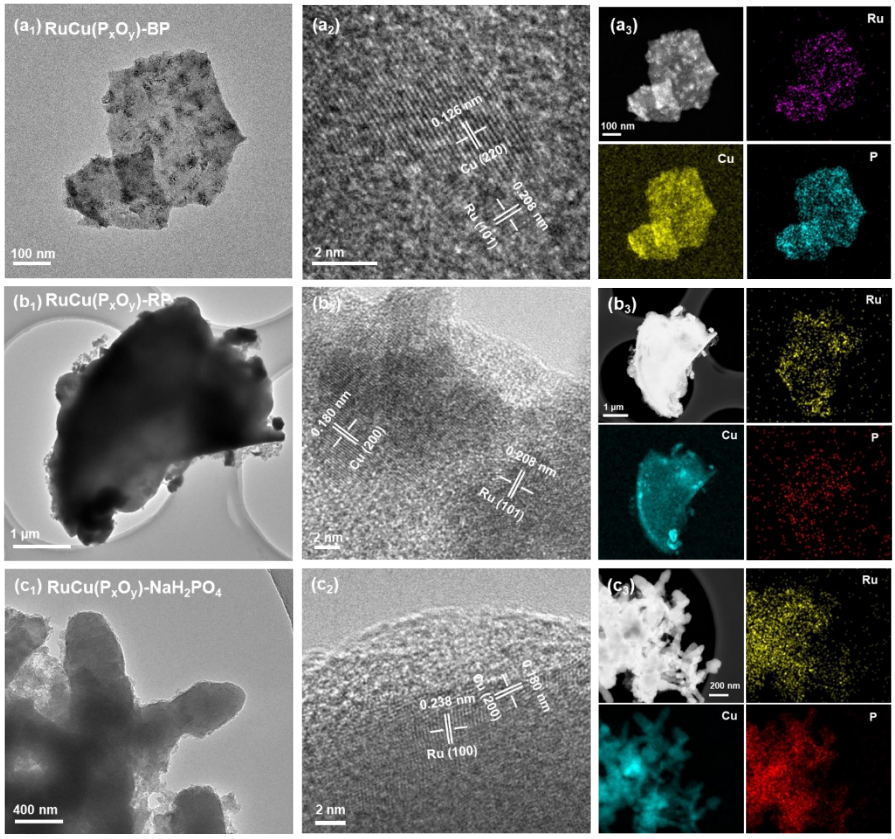

Fig. S14 TEM analyses of the (a) $RuCu(P_xO_y)$-BP, (b) $RuCu(P_xO_y)$-RP, and (c) $RuCu(P_xO_y)$-NaH_2PO_4. (a_1-c_1) TEM image, (a_2-c_2) HR-TEM image, and (a_3-c_3) HAADF-STEM and elemental mapping.

Theoretically, the interaction between P heteroatom and metal atoms modulates the d-band center position of active sites, optimizing the H* adsorption free energy to approach thermoneutrality ($\Delta G\_H \approx 0$), thereby enhancing HER kinetics[4, 5]. We further investigated the effect of P element on catalytic performance using BP, Red phosphorus (RP), and molecular phosphorus (NaH_2PO_4) as P sources, respectively. BP, as a single-element P-based 2D layered material, possesses abundant lone-pair electrons, which endow its high reactivity, enabling the potential formation of P-O-metal bonds or P-metal bonds [6]. RP exhibits no long-range crystalline order, featuring disordered molecular packing and polymeric chain structures, which is widely employed as a P precursor for the preparation of catalysts containing P heteroatom[7]. NaH_2PO_4 acts as a

P source by supplying P in the form of free $H_2PO_4^-$ ions, which can directly participate in reactions without requiring high-temperature decomposition[8].

Compared with the bulk irregular morphology of RuCu(P_xO_y)-RP and the randomly aggregated clusters of RuCu(P_xO_y)-NaH_2PO_4, the morphology of RuCu(P_xO_y)-BP has a 2D nanostructure and no discernible surface defects. The HR-TEM image of the three samples is displayed in Fig. S14. As marked, the lattice spacing of 1.26 Å and 2.08 Åcorresponds to the (220) crystal plane of Cu and (101) crystal plane of Ru, respectively. In addition, the element distribution of the three samples was further analyzed by HAADF-STEM. The elements Ru, Cu, and P were uniformly distributed on the corresponding sample surface, indicating P heteroatom was successfully incorporated into the catalyst. In addition, BP as 2D support also can utilize metal catalysts as far as possible due to the excess availability of the anchor sites[9]. This feature is beneficial for improving HER performance under alkaline medium.

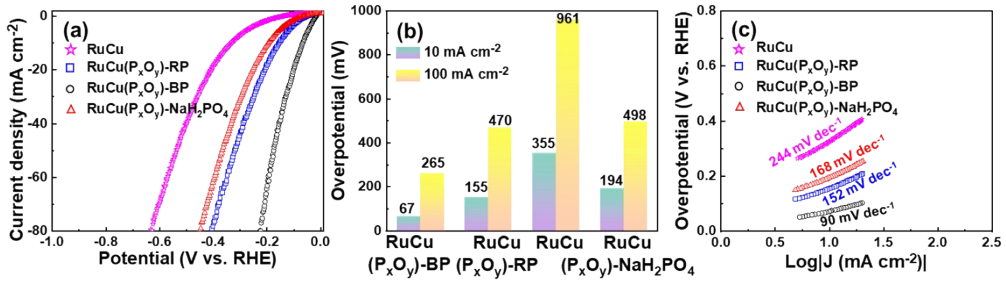

Fig. S15 HER performances of different catalysts (RuCu(P_xO_y)-BP, RuCu(P_xO_y)-RP, and RuCu(P_xO_y)-NaH_2PO_4) in an alkaline medium. (a) LSV curves, (b) Overpotential at 10 and 100 mA cm^{-2} for HER, (c) Tafel plots.

Subsequently, the effect of types of P precursors in the RuCu(P_xO_y) catalysts on catalytic activity was explored. Fig. S15 shows the LSV of RuCu(P_xO_y)-BP, RuCu(P_xO_y)-RP, RuCu(P_xO_y)-NaH_2PO_4, and RuCu catalysts in alkaline medium. As expected, RuCu(P_xO_y)-BP, RuCu(P_xO_y)-RP, and RuCu(P_xO_y)-NaH_2PO_4 catalysts exhibit markedly higher catalytic activity than PdCu catalysts. The overpotentials of RuCu(P_xO_y)-BP, RuCu(P_xO_y)-RP, and RuCu(P_xO_y)-NaH_2PO_4 require 67, 155, and 194 mV to achieve current densities of 10 mA cm^{-2} in alkaline medium, **respectively,** which is also much lower than that of RuCu (355 mV). In addition, In addition, we computed the associated Tafel slope in alkaline medium. The significantly smaller Tafel slope was observed for RuCu(P_xO_y)-BP (90 mV dec^{-1}), RuCu(P_xO_y)-RP (152 mV dec^{-1}), and RuCu(P_xO_y)-NaH_2PO_4 (168 mV dec^{-1}), in contrast to RuCu (244 mV dec^{-1}). The observed improvement in catalytic activity for RuCu(P_xO_y)-BP, RuCu(P_xO_y)-RP, and RuCu(P_xO_y)-NaH_2PO_4, relative to RuCu catalyst is presumably due to the introduction of P can optimize the H* desorption energetics at the metal sites.

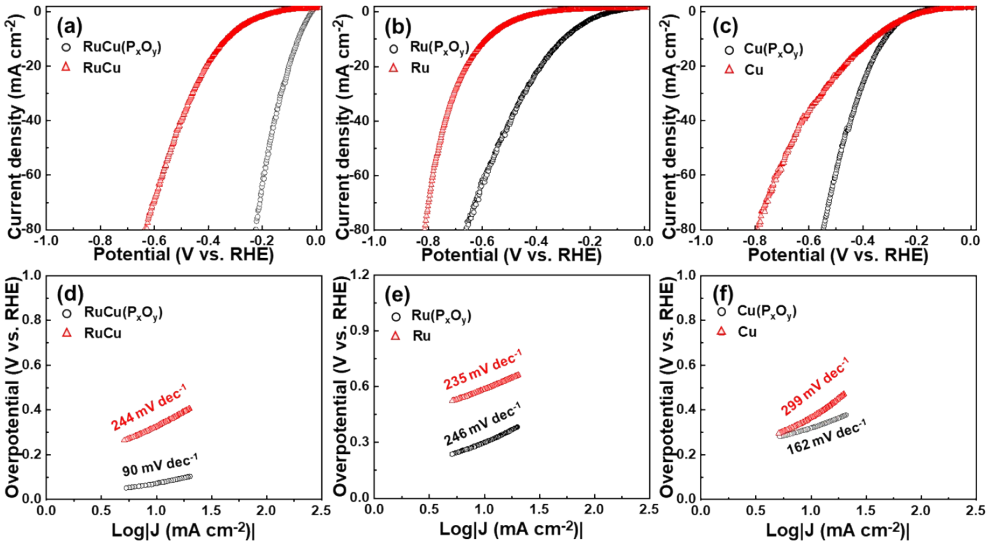

Fig. S16 HER performances of different catalysts (RuCu and RuCu(P_xO_y), Ru and Ru(P_xO_y), Cu(P_xO_y) and Cu) in an alkaline medium. (a-c) LSV curves. (d-f) Tafel plots.

We further investigated the effect of P element on the catalytic performance. The LSV polarization curves for all the samples (RuCu and RuCu(P_xO_y), Ru and Ru(P_xO_y), Cu and Cu(P_xO_y)) are illustrated in Fig. S16. The overpotentials at 10 mA cm^{-2} of the RuCu, Ru, and Cu catalysts are 335 mV, 587 mV, and 365 mV, respectively. Due to the introduction of BP, the overpotentials decreased to 67 mV (RuCu(P_xO_y)), 301 mV (Ru(P_xO_y)), and 319 mV (Cu(P_xO_y)), respectively. These results confirm that P elements are beneficial for improving HER performance under alkaline medium.

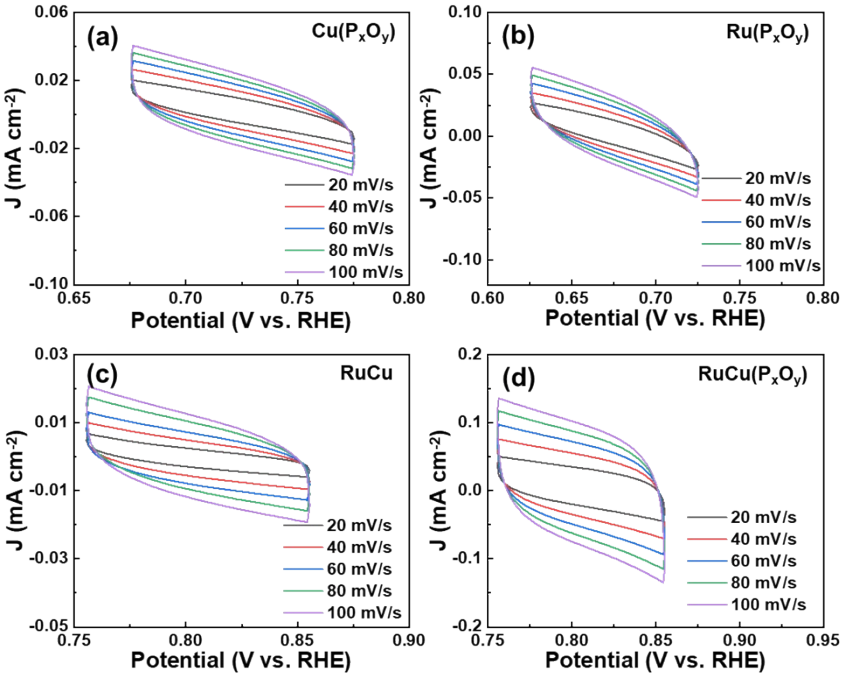

Fig. S17. CV curves of (a) $Ru(P_xO_y)$, (b) $Cu(P_xO_y)$, (c) PdCu, (d) $RuCu(P_xO_y)$ at different scan rates (20, 40, 60, 80, and 100 mV s^{-1}) under alkaline medium were obtained.

Table S1 The HER performance of different Ru-based catalysts in an alkaline medium

Catalyst	η_{10}(mV)	Tafel slope (mV dec^{-1})	Electrolyte	References
RuCu(P_xO_y)	**67**	**90**	**1.0 M KOH**	**This work**
Ru-WSe_2	87	116	1.0 M KOH	[10]
Ru@NG-10	128	104	1.0 M KOH	[11]
Ru NP@C	143	97	1.0 M KOH	[12]
$RuSe_2$@HMCS	135	106	1.0 M KOH	[13]
R-TiO_2:Ru	150	97	1.0 M KOH	[14]

Table S2 The HER performance of different catalysts in an acidic medium

Catalyst	η_{10}(mV)	Tafel slope (mV dec^{-1})	Electrolyte	References
RuCu(P_xO_y)	**83**	**77**	**0.5 M H_2SO_4**	**This work**
PY-SE-COF-Pd	128	135	0.5 M H_2SO_4	[15]
Pd/MOF	105	85	0.5 M H_2SO_4	[16]
Pd/Cu	111.5	98	0.5 M H_2SO_4	[17]
$RuSe_2$@HMCS	108	75	0.5 M H_2SO_4	[13]
Pd NWS	106	122	0.5 M H_2SO_4	[18]

Rererence

1. L. Yan, B. Zhang, S. Wu and J. Yu, *J. Mater. Chem. A*, 2020, **8**, 14234-14242.
2. B. Yang, D. Bin, Q. Zhong, B. Li, Y. Liu, H. Lu and B. Liu, *J. Colloid Interface Sci.*, 2021, **602**, 222-231.
3. J. Zhu, J. Chi, T. Cui, L. Guo, S. Wu, B. Li, J. Lai and L. Wang, *Appl. Catal. B Environ. Energy*, 2023, **328**, 122487.
4. L. Wang, W.-W. Tian, W. Zhang, F. Yu and Z.-Y. Yuan, *App. Catal. B: Environ.*, 2023, **338**, 123043.
5. S. Jiao, X. Fu and H. Huang, *Adv. Funct. Mater.*, 2022, **32**, 2107651.
6. X. Liu, L. Xiao, J. Weng, Q. Xu, W. Li, C. Zhao, J. Xu and Y. Zhao, *Sci. Adv.*, 2020, **6**, eabb4359.
7. J. M. Zaug, A. K. Soper and S. M. Clark, *Nat. Mater.*, 2008, **7**, 890-899.
8. K. Ignatova, S. Kozhukharov, M. Alakushev and Physics, *Mater. Chem. Phy.*, 2018, **219**, 175-181.
9. Z. Zhao, H. Liu, W. Gao, W. Xue, Z. Liu, J. Huang, X. Pan and Y. Huang, *J. Am. Chem. Soc.*, 2018, **140**, 9046-9050.
10. Y. Zhao, G. Mao, C. Huang, P. Cai, G. Cheng and W. Luo, *Inorg. Chem. Front.*, 2019, **6**, 1382-1387.
11. B. K. Barman, D. Das and K. K. Nanda, *Sustain. Energy Fuels* 2017, **1**, 1028-1033.
12. L.-N. Zhang, Z.-L. Lang, Y.-H. Wang, H.-Q. Tan, H.-Y. Zang, Z.-H. Kang and Y.-G. Li, *Energy Environ. Sci.*, 2019, **12**, 2569-2580.
13. F. Sun, W. Bao, C. Feng, J. Bi, C. Yue, C. Zhang, N. Liu, H. Hao and Y. Lu, *Fuel*, 2024, **370**, 131815.
14. S. Nong, W. Dong, J. Yin, B. Dong, Y. Lu, X. Yuan, X. Wang, K. Bu, M. Chen and S. Jiang, *J. Am. Chem. Soc.*, 2018, **140**, 5719-5727.
15. P. Chandrasekaran, T. N. J. I. Edison and M. G. Sethuraman, *Int. J. Hydrogen Energy*, 2020, **45**, 28800-28811.
16. J.-Y. Yue, X.-L. Ding, L.-P. Song, Y.-T. Wang, P. Yang, Y. Ma and B. Tang, *Micropor. Mesopor. Mater.*, 2022, **344**, 112169.
17. T. Chao, X. Luo, W. Chen, B. Jiang, J. Ge, Y. Lin, G. Wu, X. Wang, Y. Hu and Z. Zhuang, *Angew. Chem. Int. Ed.*, 2017, **56**, 16047-16051.
18. L. Du, D. Feng, X. Xing, C. Wang, G. S. Armatas and D. Yang, *Chem. Eng. J.*, 2020, **400**, 125864.